# Two-Dimensional Converging-Diverging Rippled Nozzles at Transonic Speeds

*John R. Carlson and Scott C. Asbury*

# Two-Dimensional Converging-Diverging Rippled Nozzles at Transonic Speeds

*John R. Carlson and Scott C. Asbury*
*Langley Research Center • Hampton, Virginia*

# Contents

# Abstract

*An experimental investigation was performed in the Langley 16-Foot Transonic Tunnel to determine the effects of external and internal flap rippling on the aerodynamics of a nonaxisymmetric nozzle. Data were obtained at several Mach numbers from static conditions to 1.2 over a range of nozzle pressure ratios. Nozzles with chordal boattail angles of 10°, 20°, and 30°, with and without surface rippling, were tested. No effect on discharge coefficient due to surface rippling was observed. Internal thrust losses due to surface rippling were measured and attributed to a combination of additional internal skin friction and shock losses. External nozzle drag for the baseline configurations were generally less than that for the rippled configurations at all free-stream Mach numbers tested. The difference between the baseline and rippled nozzle drag levels generally increased with increasing boattail angle. The thrust-minus-drag level for each rippled nozzle configuration was less than the equivalent baseline configuration for each Mach number at the design nozzle pressure ratio.*

## Introduction

Nonaxisymmetric nozzles have shown potential for improving aircraft performance and the proper design of these nozzles is crucial to efficient and effective aircraft operation (ref. 1). Flight at subsonic and low supersonic speeds can require the nozzle to have a large external closure and boattail angle due to the geometry changes in expansion ratio required for efficient operation across this range. Additionally, nozzle systems should be kept as compact as possible to minimize the weight added to the aircraft. The large aft closure can result in flow separation and excessive drag on the nozzle because external boundary layers are often unable to withstand the adverse pressure gradients in the flow over the nozzles. Nozzle design thus remains a trade-off between the higher weight and lower drag of favorable performance contours against the lower weight and higher drag of shorter nozzles.

Lobed axisymmetric structures have been used for some time in heat exchangers, transport aircraft engine fan and core flow mixers, and combustors. An axisymmetric mixer and two-dimensional (2-D) concept are shown below.
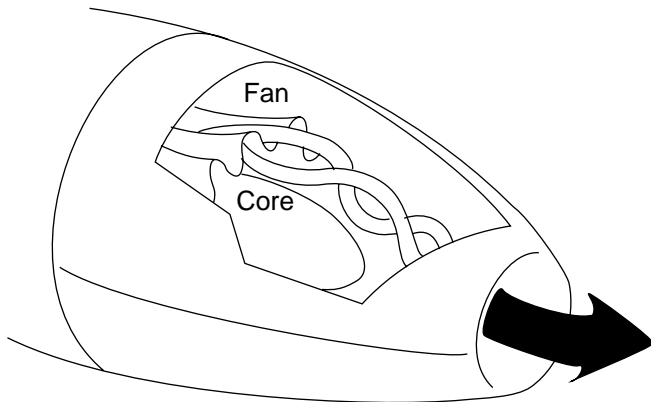


Forced mixer in a turbofan engine application.
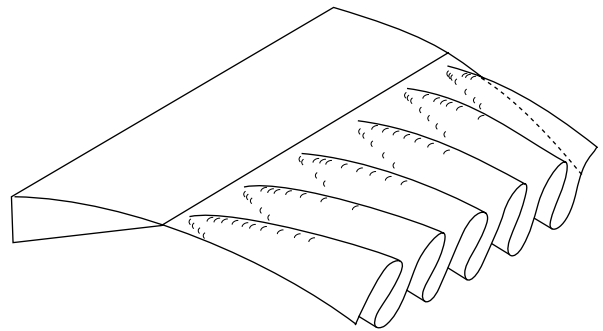
Rippled afterbody flow schematic $f$ from reference 2.

Researchers at United Technologies Research Center (UTRC) and Western New England College (WNEC) have designed an alternative shaping of an afterbody that uses a two-dimensional or non-axisymmetric version of the convoluted (rippled or lobed) trailing edge to create a more favorable pressure field for portions of the external boundary layer (ref. 2). Lobe structures were found to delay the onset of flow separation for boattail angles beyond those which would normally have some flow separation. The lobes produce transverse pressure gradients that generate secondary cross flows over the nozzle surface. These cross flows provide some pressure relief to the boundary layer in the adverse pressure gradient region approaching the nozzle trailing edge and thereby delay flow separation and reduce nozzle drag. The UTRC–WNEC investigation of the rippled nozzle was conducted in a water tunnel by using two streams with a velocity ratio of 3 and a test section Reynolds number of approximately $0.5 \times 10^6$ per foot.

The current investigation examines the merits of the lobe concept as applied to a nozzle geometry in an air (i.e., compressible) medium flowing at a higher Reynolds number than that of the water tunnel test. A rippled trailing-edge concept was applied to a nonaxisymmetric nozzle design and tested on a single-engine propulsion-simulation model in the Langley 16-Foot Transonic Tunnel. Internal and external static pressure data and isolated nozzle performance characteristics are presented for six nozzle configurations: three unrippled or baseline nozzles and three rippled nozzles. Data were obtained for nozzle chordal boattail angles of 10°, 20°, and 30° for several free-stream Mach numbers, nozzle pressure ratio settings, and model angles of attack.

## Symbols

All forces and moments are referred to the model centerline (body axis). Reference 3 contains a discussion of the data reduction procedure and definitions of the force and moment terms and the propulsion relationships.

| | |
|---|---|
| $AR_p$ | primary lobe aspect ratio, $H_L/W_p$ at exit |
| $AR_s$ | secondary lobe aspect ratio, $H_L/W_s$ at exit |
| $A_e$ | nozzle-exit area, cm$^2$ |
| $A_m$ | maximum cross-sectional area of model, cm$^2$ |
| $A_{\text{seal}}$ | cross-sectional area enclosed by seal strip at station 67.31, cm$^2$ |
| $A_t$ | nozzle-throat area, cm$^2$ |
| $a(x')$ | horizontal axis variable of superellipse geometry |
| $a_n$ | constants used in evaluating $a(x')$ |
| $b(x')$ | vertical axis variable of superellipse geometry |
| $b_n$ | constants used in evaluating $b(x')$ |
| $c$ | local chord length, cm |
| $C$ | coefficient form of quantity |
| $C_{p,n}$ | nozzle pressure coefficient, $(p - p_\infty)/q_\infty$ |
| $D_f$ | external skin-friction drag, measured from metric break (station 67.31) to nozzle connect (station 139.83), N |
| $D_n$ | nozzle drag, Pressure drag + Friction drag, N |
| $fract$ | secondary lobe geometry parameter |
| $F$ | gross thrust along body axis, N |
| $F - D$ | thrust minus drag, N |
| $F_{A,\text{mom}}$ | momentum tare axial force due to bellows, N |
| $F_{\text{bal}}$ | axial force measured by balance, N |
| $F_i$ | ideal isentropic gross thrust along body axis, N |
| $H_d$ | height of duct, cm |
| $H_L$ | height of lobe, cm |
| $H_p$ | height of primary lobe, cm |
| $H_s$ | height of secondary lobe, cm |
| $H_{\text{sp}}$ | height of splitter, cm |
| $l$ | length from nozzle-connect station to nozzle-exit station, cm |
| $M$ | free-stream Mach number |
| $N_p$ | number of primary lobes |
| $N_s$ | number of secondary lobes |
| NPR | nozzle pressure ratio, $p_{t,j}/p_\infty$ |
| $p$ | local static pressure, Pa |
| $\overline{p}_{ES}$ | average external static pressure at external seal at the metric break (station 67.31), Pa |
| $\overline{p}_i$ | average internal static pressure, Pa |

| | |
|---|---|
| $P_L$ | lobe penetration, $H_L/H_d$ |
| $p_{t,j}$ | jet total pressure, Pa |
| $q$ | dynamic pressure, Pa |
| $R$ | gas constant ($\gamma = 1.4$), 287.3 J/kg-K |
| $R_c$ | radius of corner at nozzle connect station, cm |
| $R_{\text{ext}}$ | radius of closure on external boattail, cm |
| $R_p$ | radius of primary lobe, cm |
| $R_s$ | radius of secondary lobe, cm |
| $R_{t.e.}$ | radius of corner at nozzle trailing edge, cm |
| $r'(x')$ | radius function of superellipse geometry |
| $r_c$ | nozzle circular-arc throat radius, cm |
| $t_f$ | trailing-edge thickness of nozzle flap, cm |
| $t_s$ | trailing-edge thickness of nozzle sidewall, cm |
| $T_{t,j}$ | jet total temperature, K |
| $w_i$ | ideal mass-flow rate, $\frac{\text{kg}}{\text{sec}}$ |
| $w_p$ | measured mass-flow rate, $\frac{\text{kg}}{\text{sec}}$ |
| $W_d$ | width of duct, cm |
| $W_p$ | width of primary lobe, cm |
| $W_s$ | width of secondary lobe, cm |
| $x$ | axial distance measured from nozzle connect station, positive downstream, cm |
| $x'$ | axial distance measured from apex of model nose, positive downstream, cm |
| $y$ | lateral ordinate measured from center of model, cm |
| $y'(x')$ | lateral distance from model centerline, positive up, cm |
| $z$ | vertical ordinate, cm |
| $z'(x')$ | vertical distance from model centerline, positive to right looking upstream, cm |
| $\alpha$ | model angle of attack, deg |
| $\beta_c$ | nozzle chord boattail angle measured in $x$-$z$ plane, deg |

| | |
|---|---|
| $\gamma$ | ratio of specific heats, 1.4 for air |
| $\epsilon$ | nozzle expansion ratio, $A_e/A_t$ |
| $\eta(x')$ | exponent of superellipse equation |

Abbreviations:

| | |
|---|---|
| C-D | convergent divergent |
| MS | model station |
| UTRC | United Technologies Research Center |
| 1-D | one dimensional |
| 2-D | two dimensional |
| WNEC | Western New England College |

Subscripts:

| | |
|---|---|
| $e$ | ordinates at nozzle trailing-edge station, cm |
| $t.p.$ | ordinates at external circular-arc tangent point, cm |
| $t$ | ordinates at nozzle internal throat station, cm |
| $0$ | center of external circular-arc radius, cm |
| $\infty$ | free-stream conditions |
| $F-D$ | thrust-minus-afterbody drag force measured by model balance, N |
| $F-D_n$ | thrust-minus-nozzle drag force, N |
| $D$ | afterbody drag force, N |
| $D,n$ | total nozzle drag force, N |
| $D,nf$ | nozzle external skin-friction drag force, N |
| $F,i$ | ideal thrust force, N |
| $p,n$ | nozzle external static pressure, N |

## Experimental Apparatus and Procedures

### Wind Tunnel

The single-engine propulsion-simulation model was tested in the Langley 16-Foot Transonic Tunnel. The tunnel is an atmospheric transonic single-return type with continuous air exchange and is capable of operation at Mach numbers from 0.2 to 1.3 with an accuracy of $\pm 0.005$. The average Reynolds number varies from approximately $4.5 \times 10^6$ per meter ($1.5 \times 16^6$ per foot) at a free-stream Mach number of 0.2 to approximately $12.0 \times 10^6$ per meter ($4.0 \times 10^6$ per foot) at a free-stream Mach number

of 1.3. The test section is octagonal and slotted at the vertices and has an equivalent circular diameter of 4.85 m (15.9 ft). A detailed description of the tunnel is presented in references 4 and 5.

## Propulsion Simulation System

### Single-Engine Propulsion-Simulation System

Figure 1 is a sketch of the single-engine propulsion-simulation system with a baseline two-dimensional convergent-divergent (2-D C-D) nozzle installed. The single-engine model was supported in the tunnel by a sting-strut support system, and part of the support system is shown in figure 1. The model was composed of five sections: a nose-forebody with a high-pressure plenum, a low-pressure plenum, an instrumentation section, a transition section, and a nozzle. The following table gives the model station location of each model section:

| Model section | Length, cm | Model station, cm |
|---|---|---|
| Nose-forebody | 67.31 | 0 to 67.31 |
| Low-pressure plenum | 36.70 | 67.31 to 104.01 |
| Instrumentation | 18.93 | 104.01 to 122.94 |
| Transition | 16.89 | 122.94 to 139.83 |
| Nozzle (20°) | 27.93 | 139.83 to 168.76 |

The nose-forebody was attached to the top of the strut. The forebody cross-sectional shape transitions from circular at the nose to rectangular with circular-arc corners at the metric break through a series of superelliptic curves. Geometric details of the forebody are presented in figures 2(a) and 2(b). The external centerbody of the model from station 67.31 to 139.83 was essentially rectangular in cross section and had a constant width and height of 8.636 cm and 7.874 cm, respectively. All sections of the model downstream of station 67.31 were attached to a six-component strain-gage balance. A flexible teflon seal in a circumferentially machined groove located between the nose-forebody section and low-pressure plenum minimized flow into or out of the internal cavity.

An external high-pressure air system provided a continuous flow of clean, dry air maintained at a temperature of ≈295 K. The air pressure in the instrumentation section varied up to about 83.0 kPa (≈8 atm) at a mass-flow rate of up to 5.5 kg/sec. The pressurized air was transferred from the supply source to the simulator by six air lines that run through the support strut that connect to a high-pressure plenum chamber. As shown in figure 1,

the air was then discharged perpendicularly into the model low-pressure plenum through eight multiholed sonic nozzles equally spaced around the high-pressure plenum. The high-pressure plenum was separate from the metric portion of the model. The low-pressure plenum was attached to the balance. This design attempts to minimize any forces generated by the air transferring from the nonmetric to the metric portions of the model. Two flexible metal bellows were used as seals between the metric and nonmetric portions of the model and compensated for axial forces caused from pressurization.

The air was then passed through a circular choke plate into an instrumentation section where the average total pressure and total temperature of the air was measured. The choke plate consisted of circular cross-section perforations distributed about the face of the plate with an open area of 24.858 cm$^2$ and blocked 19.1 percent of the total duct cross-sectional area at station 104.01. A transition section downstream of the instrumentation section provided a smooth transition from a circular cross-section duct to a rectangular cross-section duct to match the rectangular nozzle entrance geometry. Geometric details of the transition section are presented in figure 2(c). The same instrumentation section and choke plate were used for all calibrations and nozzles tested. All nozzles were attached to the transition section at station 139.83.

### Instrumentation

A six-component strain-gage balance was used to measure the forces and moments on the metric portion of the model. Ideal jet mass flow was determined from the average measurements of 10 total-pressure probes and 1 total-temperature probe downstream of the choke plate and just upstream of station 122.94 in the instrumentation section. The jet total pressures were measured with individual transducers mounted external to the model and support system. Actual mass flow of the high-pressure air supplied to the model was calculated from temperature and pressure measurements taken in a calibrated choked venturi system (ref. 6).

For each nozzle, external and internal static pressures were measured with surface pressure taps. (See fig. 3.) External orifices were arranged in rows along an external lobe maximum height (hill) and a lobe minimum height (valley) near the top centerline of the model and along the center of the sidewall. Three rows of orifices were similarly located internal to the nozzle. These pressures were measured with individual transducers.

4

## Test Conditions

Data were obtained at free-stream Mach numbers of 0, 0.6, 0.8, 0.9, 0.95, and 1.2 depending upon Mach number with a jet NPR range from 0 (jet off) to a maximum of 15. All nozzles were tested at an angle of attack of 0° and over a range of angle-of-attack settings at selected Mach number and NPR combinations. All tests were conducted with a boundary-layer transition strip located 2.54 cm downstream of the nose tip. The strip consisted of a 0.254-cm-wide sparse distribution of No. 100 silicon carbide grit fixed by a thin film of lacquer.

## Data Reduction

Fifty frames of data, taken at a rate of 10 frames/ sec, were averaged for each measured data parameter. A frame of data is a single reading of all tunnel and model instrumentation attached to the data acquisition system. The average values were used in subsequent calculations. Each of the six measured balance components was corrected for model weight tares, for balance component interactions, and for jet-off balance interactions resulting from the balance installation.

Two Stratford choke calibration nozzles (refs. 6 and 7) with throat areas of 25.755 cm$^2$ and 36.845 cm$^2$ were used to calibrate the model flow system. These nozzles have well-known performance characteristics over the range of nozzle internal pressures used in the facility. The calibration nozzle throat areas bracketed the throat areas of the test nozzles. Additional force corrections (tares) to the system due to the pressurized air flowing across the bellows system are determined by measuring the performance of the calibration nozzles over the range of NPR expected during the test. The resulting tare corrections were then applied to complete the corrections of the six balance components. The procedure for correcting balance measurements is documented in reference 3.

Nozzle discharge coefficient is the ratio of the measured mass-flow rate to ideal mass-flow rate ($w_p/w_i$). The ideal flow rate $w_i$ is determined by measuring the nozzle throat area and the jet total temperature and pressure in the instrumentation section upstream of the nozzle connect station, as mentioned previously, and is computed from the following equation:

$$w_i = \sqrt{\frac{\gamma}{R}\left(\frac{2}{\gamma+1}\right)^{\frac{\gamma+1}{2(\gamma-1)}}} A_t \frac{p_{t,j}}{\sqrt{T_{t,j}}}$$

The actual flow rate $w_p$, which is determined by using a multiple critical venturi system, is used to determine the ideal thrust from the following equation:

$$F_i = \sqrt{\frac{2\gamma R}{\gamma-1}}\, w_p \sqrt{T_{t,j}\left[1 - \left(\frac{p_\infty}{p_{t,j}}\right)^{\frac{\gamma-1}{\gamma}}\right]}$$

The basic data used in evaluating the isolated nozzle performance is thrust-minus-nozzle drag measured along the body axis of the model. At wind-on conditions, this parameter was obtained from the following equation:

$$F - D_n = F_{\text{bal}} + (\bar{p}_{ES} - p_\infty)(A_m - A_{\text{seal}})$$
$$+ (\bar{p}_i - p_\infty)A_{\text{seal}} + D_f - F_{A,\text{mom}}$$

The term $F_{\text{bal}}$ includes all internal and external forces on the balance. The second term represents pressure force due to the forward seal at the metric break station 76.31. The third term represents interior pressure forces. The term $D_f$ is the calculated external skin-friction drag on the constant cross-section part of the model from the metric break (station 67.31) to the start of the nozzle (station 139.83). The term $F_{A,\text{mom}}$ is the momentum tare correction determined from the calibration nozzle tests previously discussed.

The attitude of the nonmetric forebody relative to gravity was computed by a calibrated attitude indicator in the nose of the model. The angle of attack $\alpha$ was computed by correcting the model forebody attitude for centerbody deflection, due to aerodynamic loads, and for an average tunnel upflow angle of 0.1°. The accuracy of the angle-of-attack measurements was ±0.02°. The accuracies of the nondimensional force and pressures are 0.5 percent of full scale. Parameter coefficient accuracies representing 0.5-percent accuracy at full scale are as follows:

| Parameter | $M = 0.6$ | $M = 1.2$ |
|---|---|---|
| Pressure coefficient | ±0.013 | ±0.006 |
| Thrust-minus-drag ratio | ±0.016 | ±0.008 |

## Nozzle Design

The baseline geometries were chosen from the parametric nozzle study in reference 8. The parameters describing the baseline nozzles are shown in figure 4. The geometries were 2-D C-D nozzles with a circular-arc throat contour and flat divergent flaps.

The external nozzle contour consisted of a combination of a circular-arc with a straight line tangent with the arc.

The lobe cross-section methodology for the rippled nozzles was obtained from UTRC, as described in reference 2. Some terms used in the UTRC descriptions for internal mixer nozzle designs were utilized in this study, though the test media was different. The extruding (primary) lobes, normally associated with a primary flow path, are part of the internal nozzle jet stream. The inward penetrating (secondary) lobes, normally associated with a secondary or ejector stream, are immersed in the external free-stream air. A difference between these nozzles and typical mixer or ejector configurations was the absence of an external shroud surrounding the lobe structure.

The criteria chosen for the rippled nozzle design are listed as follows:

1. The upper and lower flaps at the trailing edge were not permitted to intersect each other.

2. The exit area and area distribution of the primary flow path of the rippled nozzle were the same as the respective baseline nozzle.

3. The exit geometry remained identical for all rippled nozzles. The actual length of the nozzle was a result of the chordal boattail angle.

4. For this study, $H_{sp}$ for the rippled nozzles was chosen to be the same as the height of the baseline nozzle trailing edge at the exit plane.

Though several choices of lobe penetration, lobe widths, and aspect ratios satisfy these criteria, the range of variation was limited when the rippled concept was designed to resemble an isolated 2-D C-D nozzle. Numerous combinations of these parameters can create physically unrealizable configurations; therefore, starting values for several of the parameters were obtained from a design example in the appendix of reference 2. The final parameters are tabulated in figure 5. In this study 9 primary lobes were used to approximate the 10-lobed model examined in reference 2.

Figure 5(a) shows an upper half cross-sectional view of the centerline of the 20° chord boattail rippled nozzle. The external rippling was started at the downstream circular-arc tangent point and the internal rippling was started at the location of the nozzle throat. The external tangent point of the circular-arc closure was designed to be coincident with the internal axial throat location. The contours of each baseline-rippled nozzle pair were identical upstream

of the nozzle throat location. The lobe height increased linearly from zero at the throat to its maximum height at the nozzle exit plane. Straight lines connect the trailing-edge contour with the upstream originating points and form streamwise troughs with parallel sides. A divergent internal channel occurred at the sidewall because of the divergent sidewall geometry of the baseline configuration. The external shape was developed such that there were no forward facing surfaces; that is, no surface normal vectors were oriented in the upstream direction. It was felt that any forward facing surface would excessively increase nozzle pressure drag. The primary lobe was chosen to be semicircular. The secondary lobe had to be a combination of circular corners with a flat bottom section and was determined to some degree by the primary lobe parameters. The trailing-edge geometry is shown in figures 5(b) and 5(c). The numerical definition for the rippled nozzle exit geometry is given in figure 5(c). Photographs of the nozzles installed on the wind tunnel model are shown in figures 6(a) and 6(b). Oblique views of the 10° and 30° nozzles are shown in figures 6(c) and 6(d).

## Discussion of Results

The results of this investigation are presented in both tabular and graphical form. Internal and aeropropulsive characteristics are tabulated for all configurations in tables 1 to 6, respectively. Surface pressure data are tabulated in tables 7 to 18. Graphical presentation of basic and summary data are presented as follows:

## Isolated Nozzle Performance

### Discharge Coefficient

Basic data for evaluating the isolated performance of the nozzles are presented in figure 7. Discharge coefficient $\frac{w_p}{w_i}$, which was primarily influenced by the geometry of the choke point in the nozzle, did not change significantly between the baseline and the equivalent rippled configuration for each of the three boattail angles. Each of the baseline-rippled nozzle pairs were expected to have similar mass-flow characteristics because the ripples for each set of nozzles started downstream of the geometric throat. The 10° and 20° boattail configurations maintained a discharge coefficient close to 0.992, as shown in figures 7(a) and 7(b). The discharge coefficient for the 30° boattail configuration (fig. 7(c)) was 1 percent below the level of the other two nozzles. The lower discharge coefficient of 0.982 was likely due to the extremely rapid geometric contraction just upstream of the throat that did not occur in the 10° or 20° boattail configurations.

### Static Thrust Ratio

Comparisons of the static thrust ratio for each of the baseline/rippled nozzle pairs show varying degrees of performance differences. The 10° boattail rippled nozzle static thrust at the design NPR = 6.0 was 3.4 percent below the baseline nozzle. (See fig. 7(a).) The 20° and 30° boattail rippled nozzle static thrust levels were 1.2 percent and 2 percent, respectively, below the equivalent baseline nozzle at the design NPR. (See figs. 7(b) and 7(c).) Increased skin-friction drag due to added rippled nozzle surface area was believed to be a major contributor to the differences in nozzle static thrust. However, some axial thrust loss could occur due to inviscid secondary flow losses as axial momentum is transferred to lateral momentum by the air flowing off the ridges into the valleys of the ripples.

The skin-friction contribution to the thrust loss was estimated with laminar and turbulent boundary layer theory for skin friction along a flat plate (ref. 9). The length of the plate was taken to be the same as the distance from the nozzle throat to the nozzle exit plane. An equivalent width of the plate was calculated by dividing the wetted internal area of each nozzle by the length of the plate. An internal Mach number distribution was calculated from a 1-D isentropic flow solution determined from the nozzle internal area distribution from the throat to the exit. The local Reynolds number determined from the input jet total temperature, pressure, and local Mach number was used for the local skin-friction coefficient. Transition from a laminar to a turbulent boundary layer was assumed to occur at a local Reynolds number of $0.5 \times 10^6$ and was considered fully turbulent by $2.0 \times 10^6$. The resulting integrated skin-friction force from the previous assumptions was then non-dimensionalized by the ideal thrust for that NPR. This nondimensionalization allowed for comparison of the estimated internal viscous forces in terms of thrust ratio numbers.

The 10° baseline nozzle has an estimated 0.0095 thrust ratio loss due to internal skin friction downstream of the throat as compared with the 10° rippled nozzle thrust loss of 0.0182. The higher skin-friction value appears reasonable as the rippled nozzle has slightly less than double the internal wetted area of the baseline nozzle. These estimations, though, account for less than 1/3 of the 3.4-percent performance loss between the 10° baseline and rippled nozzles. The remainder of the difference could be due to shock losses inside the narrow passages of the ripples or thrust loss due to the exhausting air not totally filling the nozzle downstream of the throat.

Estimated Thrust Loss Due to Skin Friction

[Units of $F/F_i$]

| Configuration | Baseline | Rippled |
|---|---|---|
| 10° | 0.0095 | 0.0182 |
| 20° | 0.0024 | 0.0045 |
| 30° | 0.0010 | 0.0019 |

The performance difference at NPR = 6 between the 20° baseline and rippled nozzles was approximately 1.2 percent. Roughly 1/6 of that difference can be attributed to the extra skin friction due to the ripples.

A 2-percent difference in static performance between the 30° baseline and rippled nozzles was observed at NPR = 6 with approximately 0.1 percent that could be attributed to additional skin-friction losses due to rippling.

All six nozzles were designed to have a geometric expansion ratio ($\epsilon$) of 1.48 corresponding to a design nozzle pressure ratio of 6. The data showed

that all three baseline nozzles had peak static performance occurring at the design point, as shown in the thrust ratio curves. (See fig. 7.) The thrust ratio of the 10° and 20° rippled nozzles peaked closer to NPR = 7.5 while the 30° rippled nozzle thrust ratio had not peaked by NPR = 8. Operation of the jet simulation system for static runs at these throat areas was generally restricted to nozzle pressure ratios of less than 8 because of limitations in the air system mass flow at static conditions. A design NPR = 7.5 would correspond to an expansion ratio of 1.65, approximately 11 percent above the actual geometric design point.

Several different situations could account for nozzle performance peaking at an NPR other than the design point. For example, if less throat area were available for useful air flow, the effective expansion ratio of the nozzle would be higher than the geometric expansion ratio. The fact that both the baseline and rippled nozzles had similar discharge coefficient levels over the full range of nozzle pressure ratios would discount the possibility that the ripples could have modified the character of the throat. Alternately, the same effect would occur if the actual geometric exit area were to increase due to an *oil-canning* deformation from increased internal pressure forces as NPR increased. The perimeter length of the rippled nozzle trailing edge is 103.28 cm. Deflecting the perimeter trailing edge 0.043 cm would cause an 11-percent increase in the exit area of the nozzle; however, deflections to that degree are unlikely to occur. Therefore, a third situation is postulated. Within the primary lobes, the local expansion ratio is higher than the design point of 1.48 and would have an effective design NPR that is greater than 6. Similarly, the local expansion ratio within the secondary lobe region is lower than 1.48 and the effective design NPR would be less than 6. The effective nozzle design expansion ratio could increase slightly if the influence of the primary lobes on the internal flow was greater than that of the secondary lobes. The higher thrust ratio of the 30° rippled nozzle at low NPR is probably caused by internal flow separation in the primary lobes which would have more expansion, especially for the short nozzle length created by the 30° boattail angle.

### Nozzle Drag

Figures 8 to 10 show the variation of nozzle drag coefficient $C_{D,n}$ with NPR at each Mach number at $\alpha = 0°$. Data for each baseline nozzle are compared with the corresponding rippled nozzle. Nozzle drag coefficient, composed of pressure, skin-friction, and wave drag forces, is the difference between the measured balance axial force and the static thrust of the jet. This drag force is nondimensionalized by the free-stream dynamic pressure and the maximum cross-sectional area of the body. The maximum cross-sectional area of the single-engine model is roughly 10 times smaller than a typical wing area that is normally used to nondimensionalize aerodynamic data (one airplane drag count is equivalent to 0.0001 in $C_D$). Therefore, nozzle drag coefficient levels in this paper are generally an order of magnitude greater than drag levels expressed in airplane drag counts.

The typical variation of nozzle drag with nozzle pressure ratio has a few characteristic trends. After the initial transition from jet-off to jet-on, with the subsequent drop in nozzle drag below the jet-off drag level, nozzle drag typically increases with increasing NPR settings greater than 2 where flow entrainment is the predominant influence of the jet on the external nozzle flow. As the jet NPR settings are increased beyond design, plume blockage from the expanding exhaust flow generally causes an increase in the static pressure near the nozzle trailing edge and thereby reduces the pressure drag. With all other drag components remaining relatively constant, total nozzle drag therefore decreases.

The incremental change in nozzle drag coefficient with rippling is summarized in figure 11. These data show that each rippled nozzle configuration generally has higher drag than the respective baseline nozzle and this drag difference was highest from NPR = 6 to approximately NPR = 8. The nozzle drag averaged 15 counts for the 10° configuration to roughly 100 counts for the 30° configuration. The drag difference between the baseline and rippled nozzles increases with increasing boattail angle.

### Aeropropulsive Performance With NPR

Thrust-minus-nozzle drag ratio as a function of NPR is presented in figures 12 to 14 for all six configurations. These curves are primarily influenced by the thrust characteristics of the exhaust system and in the absence of any nozzle drag become the same as the static thrust curves (or internal performance) for that nozzle. Also, as NPR is increased, thereby increasing $F_i$, the nozzle drag component $D_n/F_i$ becomes less significant and the maximum overall force ratio approaches the level of the static performance.

In general, thrust-minus-nozzle drag ratio decreases as free-stream Mach number is increased. This decrease is primarily due to the increase in external drag of the nozzle with Mach number. The subsonic performance for both the baseline

(fig. 12(a)) and rippled 10° nozzles (fig. 12(b)) were more closely grouped than the performance curves of the 20° and 30° nozzles. This close grouping indicates that the nozzle drag of the 10° boattail configurations were less sensitive to Mach number than the other two boattail angle configurations. Depending on how nozzle drag varies with NPR, the shape of the thrust-minus-drag curves can also change. Generally, internal nozzle performance is independent of Mach number, and if internal flow separation is present inside the nozzle, external flow effects could occur on nozzle thrust (ref. 10). All internal thrust data above NPR = 2 should be independent of Mach number.

## Aeropropulsive Performance With Mach Number

Figure 15 summarizes the aeropropulsive performance at $\alpha = 0$ at NPR = 0 and 6. No significant difference in nozzle drag occurred at the jet-off condition and little difference occurred at the design NPR point between the 10° baseline and rippled configurations (fig. 15(a)). As discussed previously for the static thrust comparisons, the 10° rippled nozzle thrust-minus-drag ratio was 3.4 percent below the baseline nozzle. This thrust difference was relatively constant across the range of Mach numbers tested. The absence of flow separation, which decreases the expected benefits from the rippling of the nozzle, contributed to the similarity in drag performance of the 10° nozzles at the design NPR.

Figure 15(b) is a comparison of the 20° baseline and rippled nozzles aeropropulsive performance at $\alpha = 0$ at NPR = 6. The aeropropulsive performance loss due to the rippling for the 20° nozzle was approximately 3 percent at Mach 0.6 increasing to a 6 percent loss at $M = 0.95$. Close to 16 percent in performance was lost due to rippling at Mach 1.2. The rippled nozzle drag was generally 20 percent higher than the baseline nozzle drag at the design NPR operating condition. Compared with the baseline, the rippled nozzle design had deficient nozzle aeropropulsive performance. Flow separation on the external boattail for the 20° nozzle likely occurred as the free-stream Mach number approached 0.8. The difference between the baseline and rippled nozzle thrust-minus-drag curves begins to increase after $M = 0.8$ as well. As subsequently shown, the average static pressure of the rippled nozzles appears to be lower than the baseline nozzles. This lower static pressure would contribute to a higher integrated pressure drag for the rippled nozzle. Additionally, the separation appears to occur either upstream of or close to the beginning of the nozzle ripples. The expected boundary layer energizing effects of the rip-

ples through generation of cross-flow surface velocity components, which would delay the onset of flow separation, has not had a chance to occur.

The 30° rippled nozzle installed performance loss (fig. 15(c)) varied from 4 percent at $M = 0.6$ to 11 percent at $M = 0.95$ and 9 percent at $M = 1.2$. The flow was likely separated at all conditions for both the baseline and the rippled nozzle. The rippled nozzle had either lower or comparable nozzle drag levels as the baseline nozzle at the jet-off conditions while having substantially higher drag levels for the jet operating at the design NPR. For comparison, the difference in nozzle drag levels for the rippled 10° and 20° configurations did not change significantly from jet-off to NPR = 6 over the Mach number range.

Figure 16 is a summary of the change in aeropropulsive performance due to rippling the afterbody with Mach number. All rippled configurations had losses in performance for all Mach numbers. The 10° and 20° boattail nozzles had comparable losses in performance at subsonic Mach numbers. The 30° boattail nozzle had an increasing performance penalty with increasing subsonic Mach number.

## Nozzle Internal Static Pressures

Internal static pressure distributions for each nozzle are plotted in figures 17 to 19 for a range of Mach numbers and NPR at a model angle of attack of zero. Dashed lines in the plots represent approximate location of suspected separated flow data.

### Baseline Nozzles

Internal static pressure distributions for the baseline and rippled nozzle configurations at $M = 0$ are presented in figures 17 and 18. The divergent flap and sidewall pressure distributions for the baseline configurations are fairly typical for the 2-D C-D class of nozzles. There appears to be no flow separation on the sidewalls and divergent flaps for all three nozzles (figs. 17(a) to 17(c)) except for the lowest NPR settings of NPR = 2.1. The shock-induced separation of flow from the walls of the nozzle that is typical for low NPR settings can be noted by the rapid rise in the static pressure occurring at $x/l = 0.8$ for the 10° baseline configuration (circles in fig. 17(a)) and progressing upstream to $x/l = 0.5$ for the 30° baseline configuration (circles in fig. 17(c)).

The point of sonic flow $(p/p_{t,j} = 0.528)$ on the sidewall centerline was similarly located for all baseline configurations; note the intersection of $p/p_{t,j} = 0.528$ and the static pressure distributions at $x/l$ near 0.2. The sonic point on the divergent flap moved slightly upstream of $x/l = 0.2$ for the 20° and

30° baseline configurations, though insufficient data exists to verify the exact location of this point. The additional turning of the flow into the throat to negotiate the extremely large turning angle of the 30° baseline nozzle likely overaccelerates the flow, hence the short region of compressing flow at $x/l = 0.3$, before the flow reaccelerates to the nozzle exit plane. A slight reduction in the expansion process can be noted for the 20° nozzle in the same region.

*Rippled Nozzles*

Figures 18(a) to 18(c) show internal static pressure distributions along the sidewall, the top of an internal ripple (hill), and the bottom of an internal ripple (valley) for the three rippled nozzle configurations for a range NPR exhausting under static conditions. The point of flow separation from the sidewall has moved upstream relative to the baseline nozzle distributions (compare circles of each baseline configuration of fig. 17 with the equivalent rippled configuration of fig. 18). The 30° boattail rippled nozzle sidewall flow was separated at the two lower NPR settings for approximately the complete length of the nozzle downstream of the throat. The slight divergence of the outermost rippled channel may create a more adverse pressure gradient in the vicinity of the sidewall than what occurs closer to the nozzle centerline. A slightly higher jet total pressure would therefore be required for attached flow to occur along the internal sidewalls. Despite some localized differences, the general trends and levels of the pressure distributions in the ripple hill and valley were similar. As shown in figure 19, this similarity also holds for a comparison of the baseline and rippled nozzle internal pressure distributions for NPR = 6.0.

**Nozzle External Static Pressures**

External static pressure distributions for each nozzle are plotted in figures 20 to 25 for a range of Mach numbers and NPR at a model angle of attack of zero. Figure 26 compares the baseline nozzle centerline pressure coefficients with pressure coefficient distributions along the top of an external ripple (hill) and the bottom of an external ripple (valley) of the rippled nozzle for each boattail angle configuration.

*Baseline Nozzles*

The external flow for the 10° baseline nozzle appears to have remained attached at all subsonic Mach numbers (figs. 20(a) to 20(d)) and has recovered to a positive pressure coefficient by the nozzle trailing edge. Positive pressure coefficients on this aft-facing surface area of the nozzle are beneficial in reducing the pressure drag of the nozzle. The flat pressure coefficient distribution around $x/l = 0.5$ to $x/l = 0.8$ at $M = 1.2$ (fig. 20(e)) indicates a region of possibly separated flow that still recovers, at the higher NPR conditions, to a static pressure greater than free stream in the trailing-edge region. A large pressure rise indicates the presence of a detached shock near the nozzle trailing edge that moves upstream with increasing NPR.

The pressure coefficient distributions for the 20° baseline nozzle indicate a progressively worsening pressure recovery at the nozzle trailing edge at free-stream Mach numbers beyond 0.6 (figs. 21(a) to 21(e)). The flow is probably separated from the nozzle external surface downstream of $x/l = 0.2$ for free-stream Mach numbers equal to and above 0.9 and possibly at $M = 0.8$ as well. The slight upturning of the pressure coefficient distribution downstream of $x/l = 0.7$ in figures 21(c) to 21(e) is recompression of the separated flow field toward the level of the free-stream static pressure. The flow over the 30° baseline nozzle appears to be separated downstream of $x/l = 0.2$ at all free-stream Mach numbers and jet NPR conditions. (See fig. 22.)

*Rippled Nozzles*

External pressure coefficient distributions for the three rippled nozzle configurations are shown in figures 23 to 25. Similar conclusions can be drawn for the 10° rippled nozzle configuration as discussed previously for the 10° baseline nozzle at subsonic free-stream Mach numbers. Even at the supersonic free-stream condition of $M = 1.2$, the flow separation and pressure recovery trends of the rippled nozzle are similar to those observed for the baseline nozzle.

Figure 24 shows the effect of NPR on the pressure distributions of the 20° rippled nozzle. Except for the jet-off conditions, little change occurs in the external pressure coefficient distributions with NPR downstream of $x/l = 0.4$ at $M = 0.6$ (fig. 24(a)). The peak flow acceleration near $x/l = 0.2$ does appear to be influenced to some degree by NPR changes. The effects of NPR are more pronounced as the free-stream Mach number increases. The flow appears to be separated downstream of $x/l = 0.4$ for the jet-off point and possibly separated between $x/l = 0.4$ and $x/l = 0.7$ for NPR = 2.0, as shown by the circles and squares respectively in figure 24(b). With subsequent increases in NPR, the flow may remain attached with a strong recompression trend into the nozzle trailing-edge region. The flow fails to pressurize to

greater than the free-stream static pressure for the free-stream Mach numbers above 0.9 at all the NPR conditions tested. The effect of NPR is greatest for $M = 1.2$ (fig. 24(e)), where the pressure in both the hill and the valley gradually decreases from NPR = 2 to the design point of NPR = 6. The pressure then subsequently increases until the NPR = 15 pressure distribution is roughly equivalent to the NPR = 2 pressure distribution.

External static pressure coefficient distributions for the 30° rippled nozzles are shown in figures 25(a) to 25(e). Overall, the lowest level of static pressure occurred near the design NPR at all Mach numbers. This level of pressure generally coincides with the high level of nozzle drag observed previously for this nozzle for Mach number greater than 0.8. (See squares in fig. 10.) The variation in the static pressure coefficient distributions with NPR is more pronounced as free-stream Mach number increases. The nature of the flow in the region of the nozzle trailing edge transitions from being influenced by entrainment at NPR's below the design point to being influenced by exhaust plume blockage at NPR's above the design point. The static pressure coefficient distributions in the valley were similar to those along the ripple peaks (hill). The separated region of flow appears to have totally encompassed this region of the nozzle; therefore, approximately the same static pressure was measured in the valley and hill locations.

### Comparison of External Static Pressures

*Mach = 0.6.* External static pressure coefficient distributions of each baseline nozzle compared with the corresponding rippled nozzle at NPR = 6.0 and $\alpha = 0$ are shown in figure 26 for each Mach number tested. The static pressure coefficient curves for the 10° boattail configurations at $M = 0.6$ are similar showing little difference in the magnitude of the flow expansion near $x/l = 0.2$ and the recovery pressure at the nozzle trailing edge (compare the solid circles with the open squares and diamonds in fig. 26(a)).

The curve reflex in the 20° hill pressure distribution between $x/l = 0.3$ and $x/l = 0.4$ is probably due to a slight physical slope discontinuity in the nozzle contour. The internal and external ripples start at the same streamwise location that is coincident with the internal throat and external circular-arc tangent point axial locations, as discussed previously for figure 5. The geometries of the nozzles upstream of this point are identical between the baseline and rippled configurations. The external circular-arc and straight-line intersection point is tangent only for the baseline nozzles. Consequently, the hill and valley

contours are slightly above and below the baseline contour when viewing the baseline profile imposed on the ripple profiles, respectively. All three 20° configuration distributions recovered to nearly the same positive pressure coefficient at the trailing edge.

As mentioned previously, the 30° boattail nozzle experienced external flow separation at all wind-on conditions. The baseline nozzle had a higher average static pressure from about $x/l = 0.4$ to $x/l = 0.7$. Although the rippled nozzle valley pressure recovery exceeded the baseline nozzle downstream of $x/l = 0.7$ and the rippled nozzle hill pressure recovery matched the baseline nozzle by $x/l = 0.9$, the 30° rippled nozzle drag was still higher than the baseline nozzle drag. (See fig. 11(c).) The difference between the hill and valley distributions downstream of $x/l = 0.5$ is much more pronounced for the 30° configuration than for the 10° or 20° configurations. This difference can be attributed to the greater streamwise terminal boattail angle of the valley contour compared with the hill contour.

*Mach = 0.8.* The results of the comparison of the baseline nozzle with rippled nozzle pressure distributions for the 10° boattail nozzle were not significantly different at $M = 0.8$ than at $M = 0.6$. The flow over the 20° boattail nozzle possibly has a region of separated flow as evidenced by the greatly diminished negative pressure coefficient peak at $x/l = 0.2$ (compare with the pressure coefficient distribution at $M = 0.6$). Attached flow accelerates strongly around the initial closure of the nozzle and this typically results in a relatively high negative pressure coefficient around $x/l = 0.1$ to $0.2$. Though insufficient pressure data were obtained, the flow likely has a shock-induced separation at or just upstream of $x/l = 0.2$. Results obtained for the 30° boattail nozzle at $M = 0.8$ were similar to those discussed previously for the nozzle at $M = 0.6$.

*Mach = 0.9 and 0.95.* The 10° configurations show little difference at a free-stream Mach number of 0.9 (fig. 26(c)). Both 20° nozzles appear to be separated by $M = 0.9$. The rippled nozzle hill flow compresses slightly more than the baseline nozzle flow upstream of $x/l = 0.4$ and expands slightly more than the baseline flow downstream of $x/l = 0.4$. However, the valley pressure distribution is not significantly different from that of the baseline. The 30° baseline and rippled configurations appear to be separated with the average static pressure of the rippled configuration lower than the baseline.

*Mach = 1.20.* As discussed previously, the differences between the external pressure distributions of

the baseline and rippled nozzle configurations for the 10° boattail are fairly small even at a free-stream Mach number of 1.2 (fig. 26(e)). A comparison of the 20° boattail nozzle pressure distributions show, in general, lower static pressure coefficients along the full length of the rippled configuration than along the baseline configuration. Similar levels of static pressure coefficients were not attained on the 20° boattail rippled nozzle unless the NPR was either very low (i.e., NPR = 2.0) or very high (i.e., NPR = 15.0). The flow over both of the 30° boattail configurations appears to be separated at $M = 1.2$ with no benefit being derived from the rippling of the nozzle.

## Concluding Remarks

An experimental investigation was performed to determine the effects of external and internal rippling on the aerodynamics of a nonaxisymmetric nozzle. Data were obtained at several Mach numbers from static conditions to 1.2 over a range of nozzle pressure ratios (NPR's). Nozzles with chordal boattail angles of 10°, 20°, and 30° with and without surface rippling were tested. The results are as follows:

1. Rippling nonaxisymmetric nozzle divergent flaps downstream of the throat had little or no effect on the internal mass-flow characteristics of the nozzle.

2. The static thrust ratio of each rippled nozzle varied from ≈1 to ≈3 percent less than the equivalent baseline nozzle configuration. Typically, less than ≈1/3 of the difference in thrust could be attributed to additional skin-friction drag due to the additional internal surface area from the rippling of the nozzles.

3. The nozzle drag was generally less for the baseline configurations than for the rippled configurations at all free-stream Mach numbers tested, and the nozzle drag averaged 15 counts for the 10° configuration to roughly 100 counts for the 30° configuration. The difference between the drag levels for the baseline and rippled nozzle increased with increasing boattail angle.

4. Extensive external flow separation was indicated for nozzles that have boattail angles of ≈20° and ≈30°. This separation may have occurred at or upstream of the start of the nozzle ripples, thus precluding any potential benefits from the rippled surfaces.

The occurrence of the external flow separation upstream of the ripples indicates that the first area of

attention for the redesign of the rippled afterbody should be advancing the start of the rippling upstream of the start of the nozzle closure and flow separation. Other considerations should be to design for a larger number of primary lobes of lower height to possibly work more in the boundary layer of the external flow as well as to delay the start of the internal ripples to attempt to decrease the internal performance losses.

NASA Langley Research Center
Hampton, VA 23681-0001
March 8, 1994

## References

1. Capone, Francis J.: The Nonaxisymmetric Nozzle—It Is for Real. AIAA-79-1810, Aug. 1979.

2. Presz, Walter M., Jr.; Russell, William D.; and Tongue, Steve E.: *Rippled Afterbody Performance Study.* UTRC87-27, Sept. 1987.

3. Mercer, Charles E.; Berrier, Bobby L.; Capone, Francis J.; and Grayston, Alan M.: *Data Reduction Formulas for the 16-Foot Transonic Tunnel—NASA Langley Research Center, Revision 2.* NASA TM-107646, 1992.

4. Corson, Blake W., Jr.; Runckel, Jack F.; and Igoe, William B.: *Calibration of the Langley 16-Foot Transonic Tunnel With Test Section Air Removal.* NASA TR R-423, 1974.

5. Staff of the Propulsion Aerodynamics Branch: *A User's Guide to the Langley 16-Foot Transonic Tunnel Complex, Revision 1.* NASA TM-102750, 1990. (Supersedes NASA TM-83186, compiled by Kathryn H. Peddrew, 1981.)

6. Berrier, Bobby L.; Leavitt, Laurence D.; and Bangert, Linda S.: *Operating Characteristics of the Multiple Critical Venturi System and Secondary Calibration Nozzles Used for Weight-Flow Measurements in the Langley 16-Foot Transonic Tunnel.* NASA TM-86405, 1985.

7. Stratford, B. S.: The Calculation of the Discharge Coefficient of Profiled Choked Nozzles and the Optimum Profile for Absolute Air Flow Measurement. *J. R. Aeronaut. Soc.*, vol. 68, no. 640, Apr. 1964, pp. 237–245.

8. Pendergraft, Odis C., Jr.; Burley, James R., II; and Bare, E. Ann: *Parametric Study of Afterbody/Nozzle Drag on Twin Two-Dimensional Convergent-Divergent Nozzles at Mach Numbers From 0.60 to 1.20.* NASA TP-2640, 1986.

9. Schlichting, Hermann (J. Kestin, transl.): *Boundary-Layer Theory,* Seventh ed. McGraw-Hill Book Co., 1979.

10. Berrier, Bobby L.; and Re, Richard J.: *Investigation of Convergent-Divergent Nozzles Applicable to Reduced-Power Supersonic Cruise Aircraft.* NASA TP-1766, 1980.

(a) Nose-forebody section with equations and table defining external geometry.

Figure 2. External geometry of nose-forebody section. All dimensions are in centimeters unless otherwise noted.

(c) Transition section with equations and table defining the internal geometry.

Figure 2. Concluded.

(a) Lower-quarter view of 30° rippled nozzle installed on model.

(b) Side-oblique view of 10° rippled nozzle installed on model.

Figure 6. Photographs of wind tunnel model.

L-92-00579

L-92-00668

L-91-11028

L-91-11031

(c) 30° baseline and rippled nozzles.

(d) 10° baseline and rippled nozzles.

Figure 6. Concluded.

(a) 10° nozzles.

(b) 20° nozzles.

Figure 7. Nozzle static performance.

(c) 30° nozzles.

Figure 7. Concluded.

(a) $M = 0.60$ to $0.90$.

Figure 8. Variation of nozzle drag coefficient with NPR for 10° nozzles at $\alpha = 0°$.

(b) $M = 0.95$ and $1.20$.

Figure 8. Concluded.

(a) $M = 0.60$ to $0.90$.

Figure 9. Variation of nozzle drag coefficient with NPR for 20° nozzles at $\alpha = 0°$.

(b) $M = 0.95$ and $1.20$.

Figure 9. Concluded.

(a) $M = 0.60$ to $0.90$.

Figure 10. Variation of nozzle drag coefficient with NPR for 30° nozzles at $\alpha = 0°$.

(b) $M = 0.95$ and $1.20$.

Figure 10. Concluded.

(a) 10° baseline nozzle.

(b) 10° rippled nozzle.

Figure 12. Variation of thrust-minus-drag ratio with NPR for 10° nozzles at $\alpha = 0°$.

(a) 20° baseline nozzle.

(b) 20° rippled nozzle.

Figure 13. Variation of thrust-minus-drag ratio with NPR for 20° nozzles at $\alpha = 0°$.

(a) 30° baseline nozzle.

(b) 30° rippled nozzle.

Figure 14. Variation of thrust-minus-drag ratio with NPR for 30° nozzles at $\alpha = 0°$.

(a) 10° nozzles.

Figure 15. Summary of nozzle aeropropulsive performance characteristics with $\alpha = 0°$.

(b) 20° nozzles.

Figure 15. Continued.

(c) 30° nozzles.

Figure 15. Concluded.

(a) 10° baseline nozzle.

(b) 20° baseline nozzles.

Figure 17. Effect of NPR on internal static pressure distributions of baseline nozzles with $M = 0$.

(c) 30° baseline nozzles.

Figure 17. Concluded.

(a) 10° rippled nozzle.

Figure 18. Effect of NPR on internal static pressure distributions of the rippled nozzles with $M = 0$.

(b) 20° rippled nozzle.

Figure 18. Continued.

(c) 30° rippled nozzle.

Figure 18. Concluded.

(a) 10° nozzle boattail.

(b) 20° nozzle boattail.

Figure 19. Baseline and rippled nozzle internal pressure distributions at nominal NPR = 6.0 and $M = 0$.

(c) 30° nozzle boattail.

Figure 19. Concluded.

(a) Mach = 0.60.

(b) Mach = 0.80.

Figure 20. Nozzle pressure coefficient distributions for the 10° baseline nozzle at $\alpha = 0°$.

(c) Mach = 0.90.

(d) Mach = 0.95.

Figure 20. Continued.

(e) Mach = 1.20.

Figure 20. Concluded.
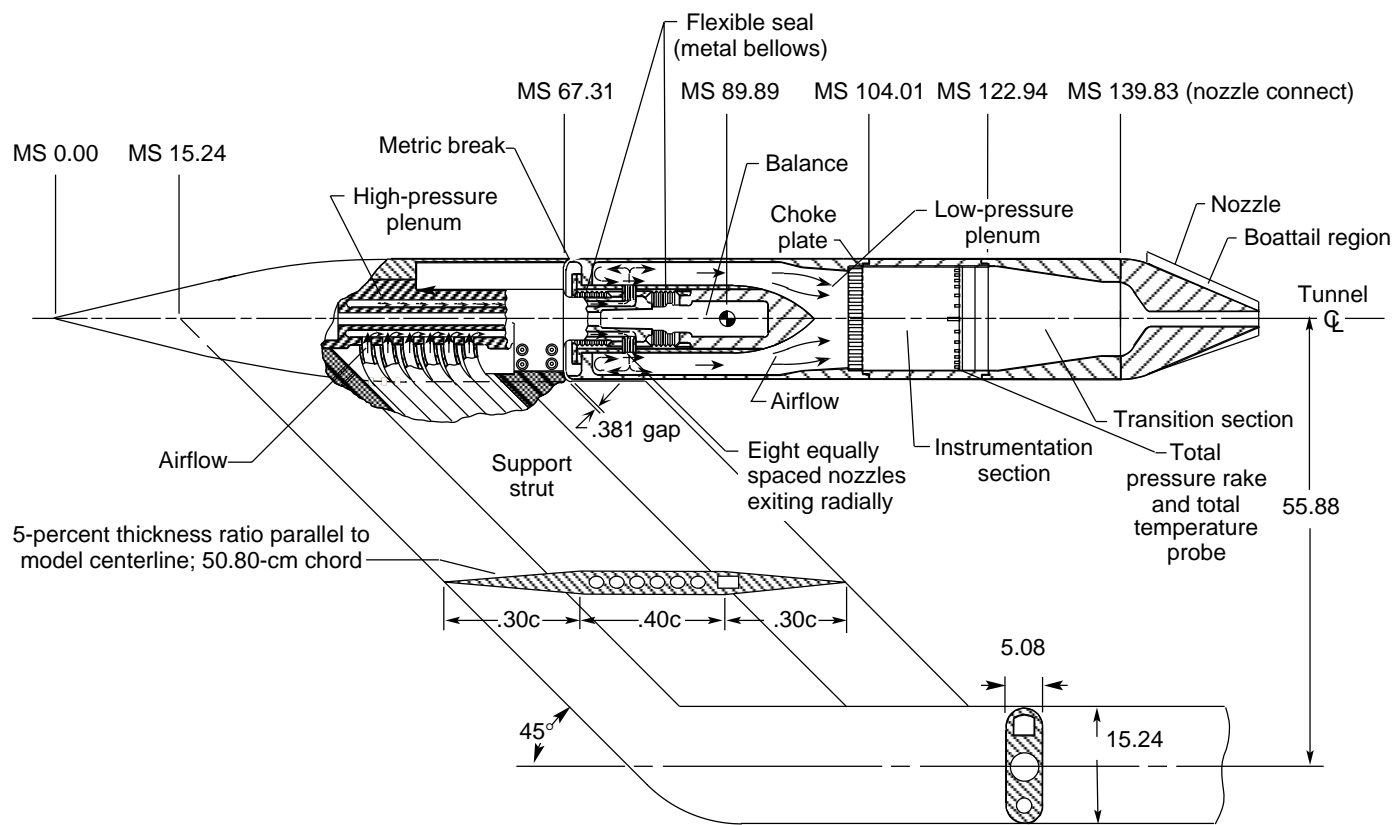
Figure 1. Air-powered nacelle model with nonaxisymmetric nozzle installed. All dimensions are in centimeters unless otherwise noted.
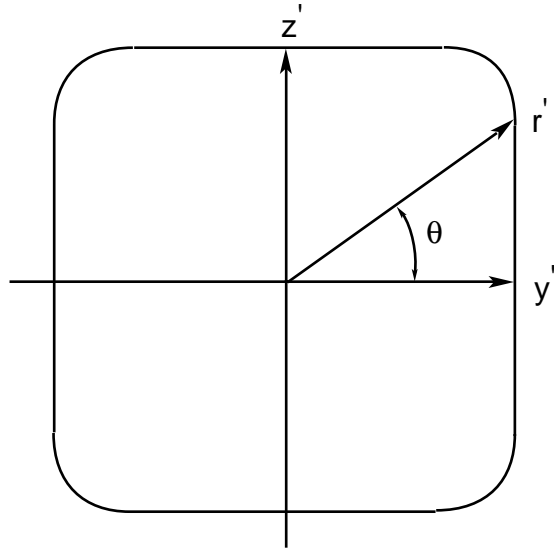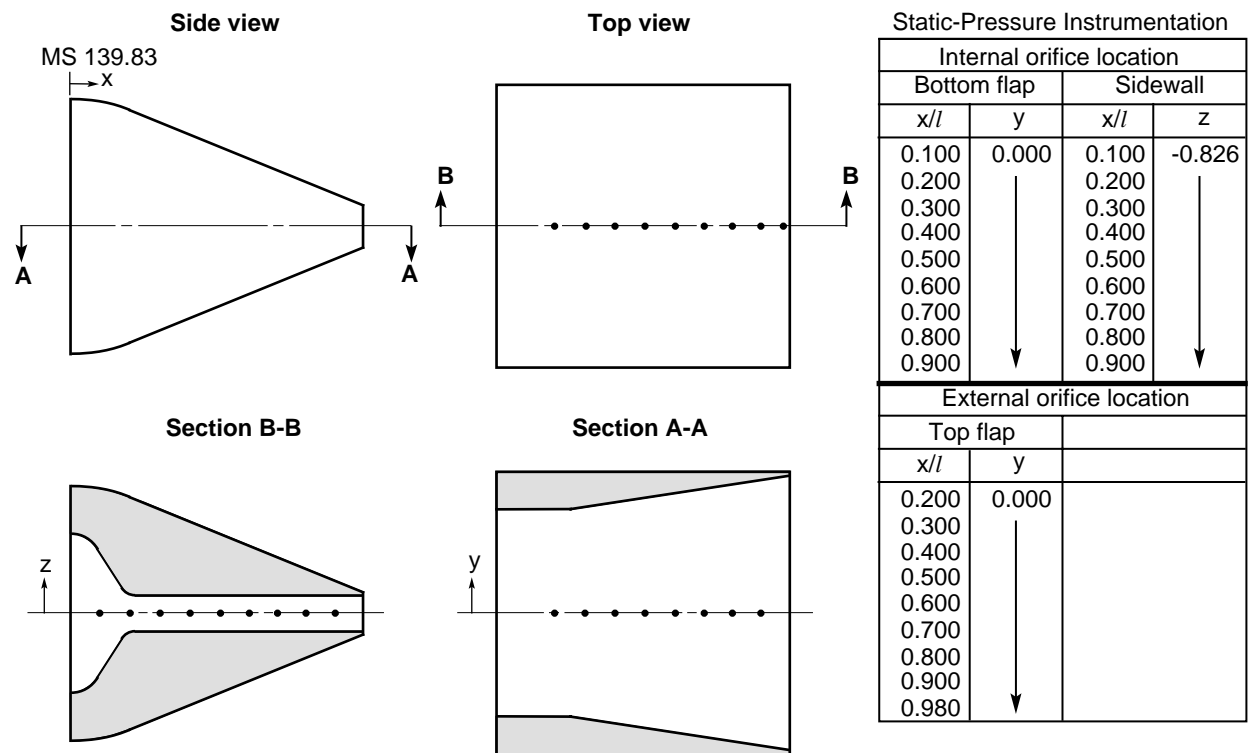
$$y'(x') = r'(x') \cos \theta \qquad\qquad z'(x') = r'(x') \sin \theta$$

$$r'(x') = \left\{ \left[ \frac{\cos \theta}{a^{(x')}} \right]^{\eta(x')} + \left[ \frac{\sin \theta}{b\,(x')} \right]^{\eta(x')} \right\}^{-1/\eta(x')}$$

(b) Superellipse cross section at constant value of $x'$, looking upstream.

Figure 2. Continued.

**Side view**

MS 139.83

**Top view**

**Static-Pressure Instrumentation**

| Internal orifice location | | | |
|---|---|---|---|
| Bottom flap | | Sidewall | |
| $x/l$ | $y$ | $x/l$ | $z$ |
| 0.100 | 0.000 | 0.100 | -0.826 |
| 0.200 | | 0.200 | |
| 0.300 | | 0.300 | |
| 0.400 | | 0.400 | |
| 0.500 | | 0.500 | |
| 0.600 | | 0.600 | |
| 0.700 | | 0.700 | |
| 0.800 | | 0.800 | |
| 0.900 | | 0.900 | |

**Section B-B**

**Section A-A**

| External orifice location | | | |
|---|---|---|---|
| Top flap | | | |
| $x/l$ | $y$ | | |
| 0.200 | 0.000 | | |
| 0.300 | | | |
| 0.400 | | | |
| 0.500 | | | |
| 0.600 | | | |
| 0.700 | | | |
| 0.800 | | | |
| 0.900 | | | |
| 0.980 | | | |

(a) Baseline nozzles.

Figure 3. Static-pressure orifice locations. (Filled circles denote orifice location.) All dimensions are in centimeters unless otherwise noted.

## Side view

MS 139.83

**Section B-B**

**Top view**

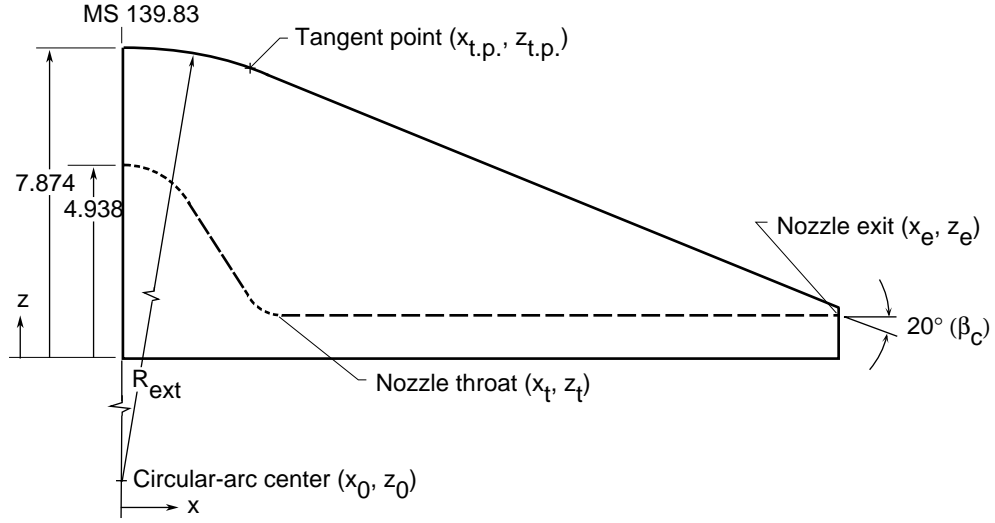**Section A-A**

## Static-Pressure Instrumentation

| Internal orifice location | | | | | |
|---|---|---|---|---|---|
| Bottom flap | | | | Sidewall | |
| Hill | | Valley | | | |
| x/l | y | x/l | y | x/l | z |
| 0.150 | 1.031 | 0.150 | 0.000 | 0.100 | -0.826 |
| 0.200 | ↓ | 0.200 | ↓ | 0.200 | ↓ |
| 0.300 | | 0.300 | | 0.300 | |
| 0.400 | | 0.400 | | 0.400 | |
| 0.500 | | 0.500 | | 0.500 | |
| 0.600 | | 0.600 | | 0.600 | |
| 0.700 | | 0.700 | | 0.800 | |
| 0.800 | | 0.800 | | 0.900 | |
| | | 0.900 | | 0.980 | |

| External orifice location | | | | |
|---|---|---|---|---|
| Top flap | | | | |
| Hill | | Valley | | |
| x/l | y | x/l | y | |
| 0.200 | 0.000 | 0.100 | -1.031 | |
| 0.300 | ↓ | 0.200 | ↓ | |
| 0.400 | | 0.300 | | |
| 0.500 | | 0.400 | | |
| 0.600 | | 0.500 | | |
| 0.700 | | 0.600 | | |
| 0.800 | | 0.700 | | |
| 0.900 | | 0.800 | | |
| 0.980 | | 0.900 | | |

(b) Rippled nozzles.

Figure 3. Concluded.

54

(a) Sketch of upper half of 20° baseline nozzle.

| $\beta_c$, deg | External geometry | | | | | Internal geometry | | | | | |
|---|---|---|---|---|---|---|---|---|---|---|---|
| | $R_{ext}$ | $x_0$ | $z_0$ | $x_{t.p.}$ | $z_{t.p.}$ | $x_t$ | $y_t$ | $z_t$ | $x_e$ | $y_e$ | $z_e$ |
| 10 | 43.492 | 0.0 | -35.618 | 8.509 | 7.034 | 8.057 | 6.286 | 1.092 | 36.995 | 8.382 | 1.351 |
| 20 | 10.790 | 0.0 | -2.915 | 4.122 | 7.055 | 4.188 | 6.286 | 1.094 | 17.922 | 8.382 | 1.351 |
| 30 | 4.717 | 0.0 | 3.157 | 2.598 | 7.094 | 2.862 | 6.286 | 1.085 | 11.298 | 8.382 | 1.351 |

(a) Sketch of upper half of 20° baseline nozzle.
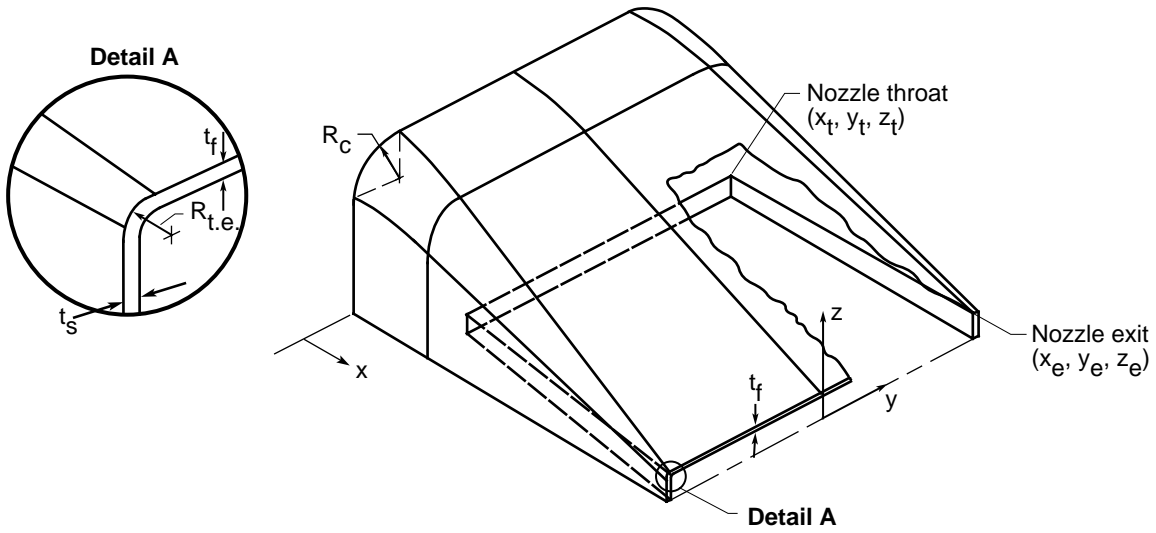


(b) Sketch of upper half of 20° baseline nozzle.

Figure 4. Description of baseline nozzle geometries. All dimensions are in centimeters unless otherwise noted.

55
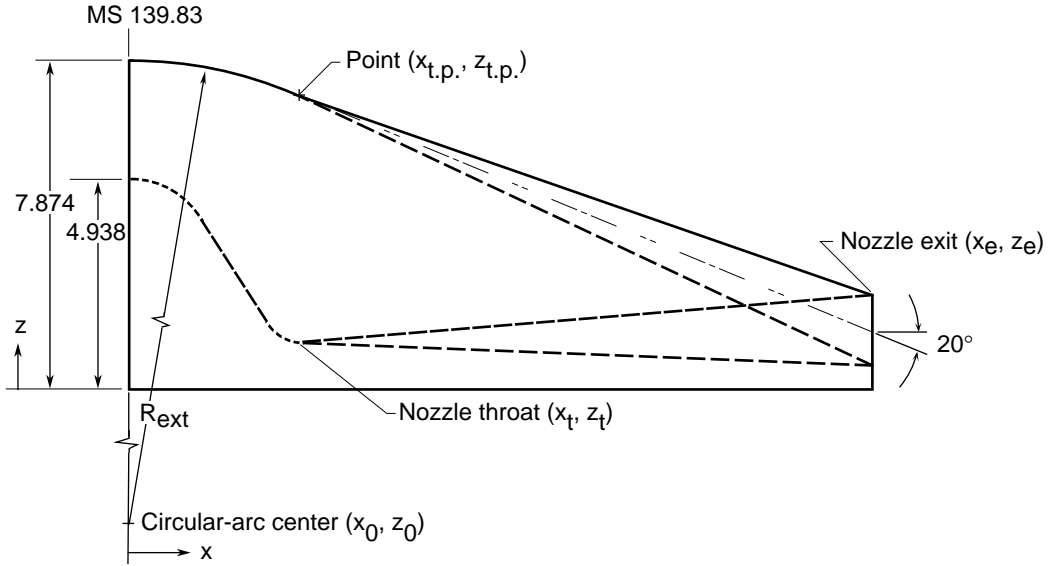
| 10° baseline nozzle | | 20° baseline nozzle | | 30° baseline nozzle | |
| --- | --- | --- | --- | --- | --- |
| X | Z | X | Z | X | Z |
| 0.000 | 4.938 | 0.000 | 4.938 | 0.000 | 4.938 |
| 0.447 | 4.933 | 0.491 | 4.935 | 0.240 | 4.932 |
| 0.848 | 4.918 | 0.710 | 4.925 | 0.374 | 4.930 |
| 1.245 | 4.857 | 0.929 | 4.893 | 0.526 | 4.929 |
| 1.636 | 4.755 | 1.149 | 4.832 | 0.710 | 4.899 |
| 2.011 | 4.613 | 1.359 | 4.736 | 0.889 | 4.818 |
| 2.368 | 4.435 | 1.557 | 4.602 | 1.034 | 4.696 |
| 2.708 | 4.231 | 1.725 | 4.444 | 1.141 | 4.562 |
| 3.030 | 4.007 | 1.864 | 4.265 | 1.225 | 4.420 |
| 3.338 | 3.769 | 1.979 | 4.080 | 1.346 | 4.140 |
| 3.636 | 3.520 | 2.160 | 3.693 | 1.474 | 3.719 |
| 3.925 | 3.266 | 2.364 | 3.112 | 1.597 | 3.164 |
| 4.209 | 3.010 | 2.425 | 2.922 | 1.625 | 3.026 |
| 4.491 | 2.757 | 2.550 | 2.544 | 1.683 | 2.753 |
| 4.775 | 2.507 | 2.616 | 2.364 | 1.712 | 2.618 |
| 5.062 | 2.266 | 2.772 | 2.015 | 1.806 | 2.215 |
| 5.357 | 2.037 | 2.862 | 1.857 | 1.925 | 1.835 |
| 5.660 | 1.823 | 3.082 | 1.568 | 2.030 | 1.603 |
| 5.972 | 1.631 | 3.209 | 1.447 | 2.162 | 1.394 |
| 6.295 | 1.461 | 3.351 | 1.340 | 2.236 | 1.309 |
| 6.630 | 1.320 | 3.504 | 1.253 | 2.412 | 1.174 |
| 6.975 | 1.211 | 3.666 | 1.184 | 2.513 | 1.129 |
| 7.328 | 1.136 | 3.836 | 1.136 | 2.615 | 1.102 |
| 7.687 | 1.099 | 4.012 | 1.108 | 2.732 | 1.089 |
| 8.057 | 1.092 | 4.188 | 1.094 | 2.862 | 1.085 |

(a) Sketch of upper half of 20° rippled nozzle and upstream throat coordinates.

Figure 5. Description of rippled nozzle geometries.
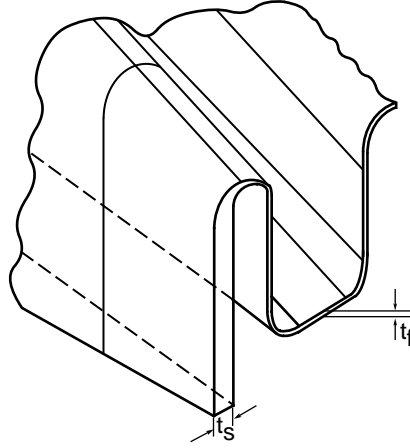
(b) Oblique sketch of rippled nozzle geometry showing details of sidewall lobe at exit plane.
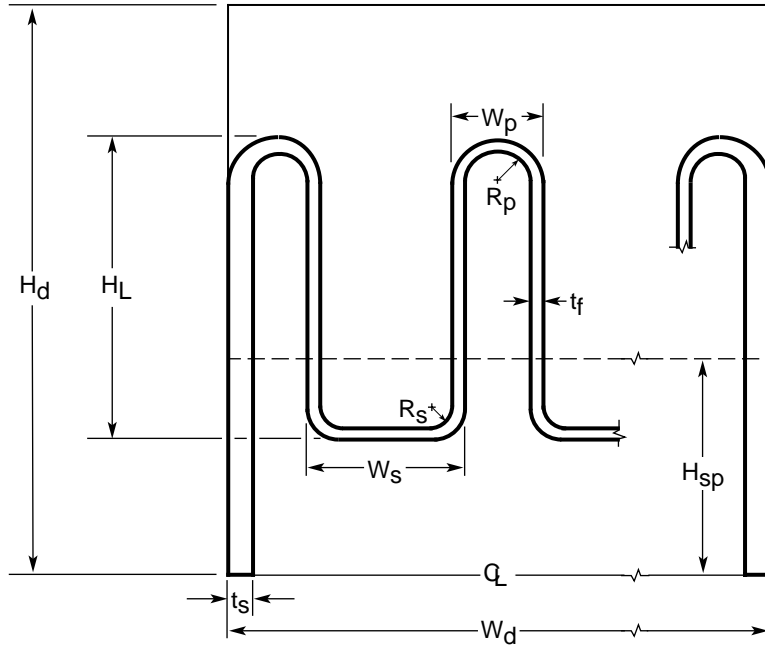


| Parameter | Baseline | Rippled |
|---|---|---|
| $AR_p$ | | 3.000 |
| fract | 0 | 0.300 |
| $H_d$ | 7.874 | 7.874 |
| $H_{sp}$ | 1.351 | 1.351 |
| $N_p$ | | 9.000 |
| $P_L$ | | 0.300 |
| $R_c$ | 0.254 | 0.254 |
| $R_p$ | | 0.236 |
| $R_s$ | | 0.420 |
| $t_f$ | 0.142 | 0.064 |
| $t_s$ | 0.254 | 0.254 |
| $W_d$ | 17.272 | 17.272 |
| $W_s$ | | 1.400 |
| $H_L/H_d$ | 0 | 0.300 |
| $H_L/W_p$ | 0 | 3.000 |
| $H_L/W_s$ | 0 | 1.517 |

$$N_s = N_p - 1$$
$$H_L = P_L H_d$$
$$W_p = P_L H_d / AR_p$$
$$W_{pr} = W_p/2$$
$$W_s = (W_d = 2N_s t_f - N_p W_p)/N_s$$
$$AR_s = P_L H_d / W_s$$

$$W_{sr} = (fract)(W_s)$$
$$t_p = \pi W_{pr}^2/2$$
$$b_p = \pi W_{sr}^2/2 + (W_s - 2W_{sr})(W_{sr})$$
$$t_{tp} = \pi(W_{pr} - t_f)^2/2$$
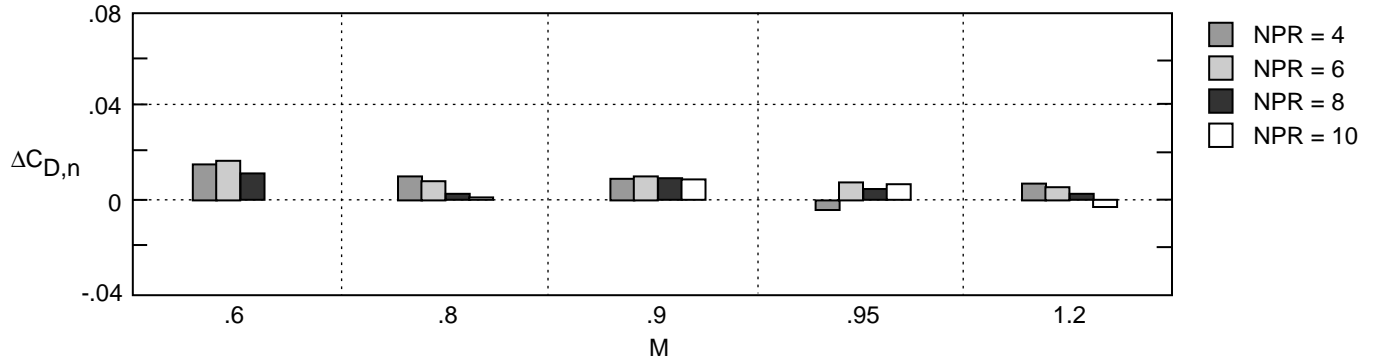$$t_{bp} = \pi(W_{sr} - t_f)^2/2 + (W_s - 2W_{sr})(W_{sr} - t_f)$$
$$H_{ratio} = H_{sp}/(H_d - H_{sp})$$

$$H_p = -\frac{[(N_s t_{bp} + N_s t_p + H_{ratio}(N_p t_{tp} - N_s b_p) - (H_L - 2t_f - W_{pr} - W_{sr})(N_s W_s + H_{ratio} N_s W_s + N_s 2t_f)]}{[N_p W_p + H_{ratio} N_p W_p + H_{ratio}(N_p 2t_f + N_s W_s) + N_s W_s + N_s 2t_f]}$$

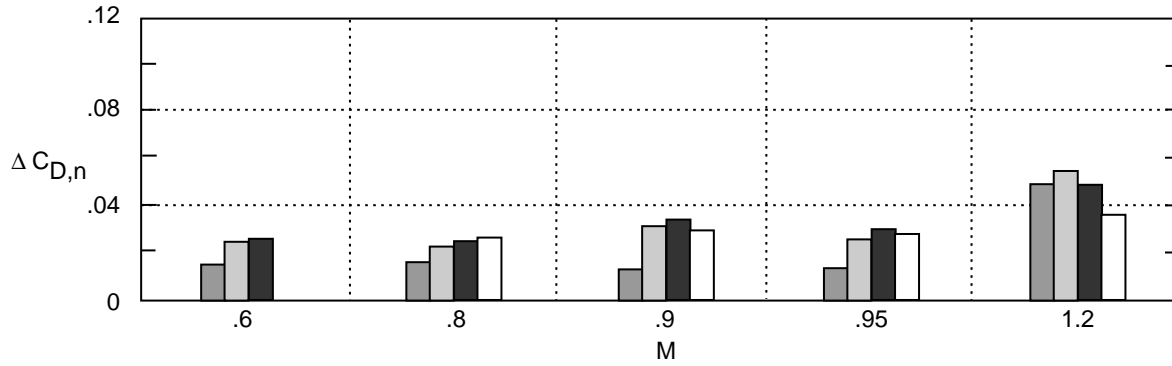$$H_s = H_L - 2t_f - W_{pr} - W_{sr} - W_{sr} - H_p$$

(c) Lobe parameters at nozzle trailing edge, reproduced from reference 2.
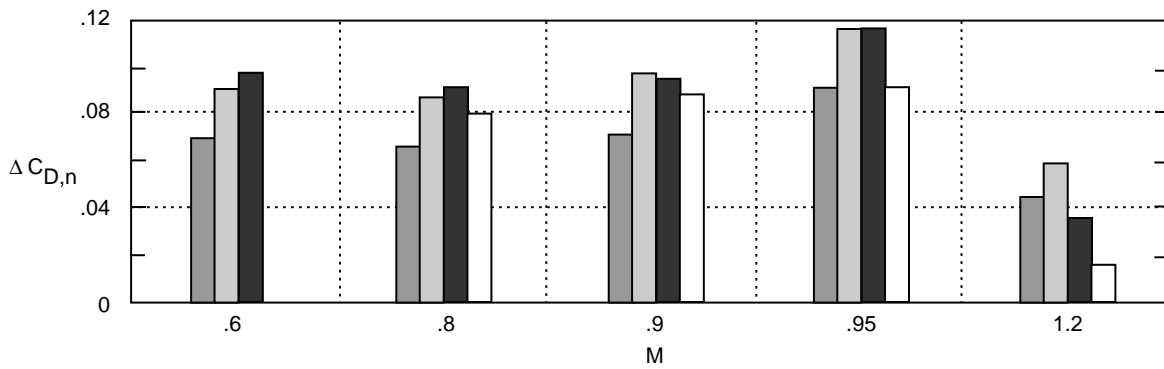
Figure 5. Concluded.

57

(a) 10° boattail.



(b) 20° boattail.



(c) 30° boattail.

Figure 11. Increment in nozzle $C_{D,n}$ due to nozzle ripple contours.

Figure 16. Increment in installed performance due to rippled contours.
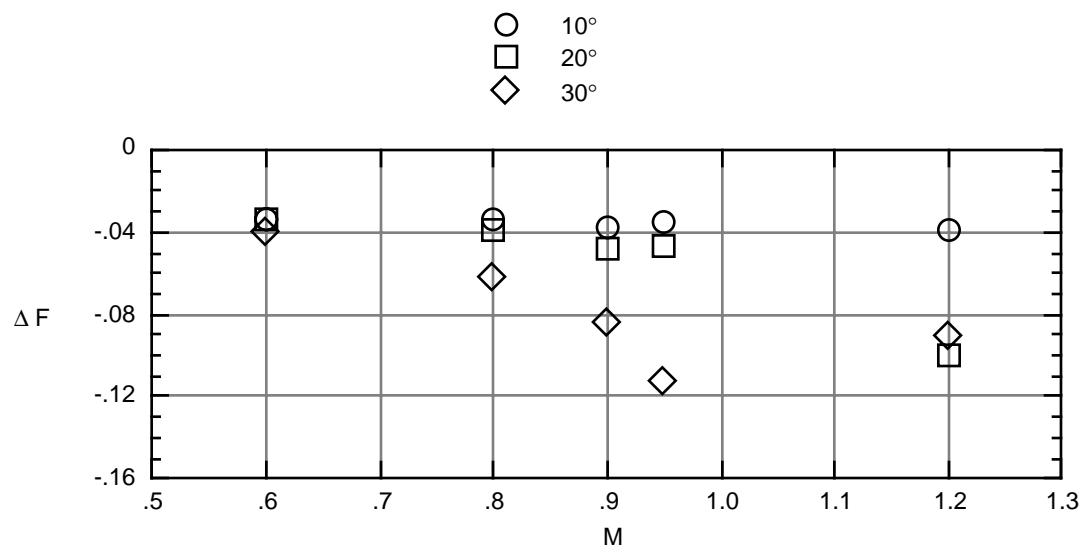
$\Delta F = (Rippled - Baseline)\ (F\text{-}Dn)/Fi$

NPR = 6; $\alpha = 0$

# REPORT DOCUMENTATION PAGE

Public reporting burden for this collection of information is estimated to average 1 hour per response, including the time for reviewing instructions, searching existing data sources, gathering and maintaining the data needed, and completing and reviewing the collection of information. Send comments regarding this burden estimate or any other aspect of this collection of information, including suggestions for reducing this burden, to Washington Headquarters Services, Directorate for Information Operations and Reports, 1215 Jefferson Davis Highway, Suite 1204, Arlington, VA 22202-4302, and to the Office of Management and Budget, Paperwork Reduction Project (0704-0188), Washington, DC 20503.

| 1. AGENCY USE ONLY *(Leave blank)* | 2. REPORT DATE<br>July 1994 | 3. REPORT TYPE AND DATES COVERED<br>Technical Paper |
|---|---|---|

**4. TITLE AND SUBTITLE**
Two-Dimensional Converging-Diverging Rippled Nozzles at Transonic Speeds

**5. FUNDING NUMBERS**
WU 505-62-30-01

**6. AUTHOR(S)**
John R. Carlson and Scott C. Asbury

**7. PERFORMING ORGANIZATION NAME(S) AND ADDRESS(ES)**
NASA Langley Research Center
Hampton, VA 23681-0001

**8. PERFORMING ORGANIZATION REPORT NUMBER**
L-17265

**9. SPONSORING/MONITORING AGENCY NAME(S) AND ADDRESS(ES)**
National Aeronautics and Space Administration
Washington, DC 20546-0001

**10. SPONSORING/MONITORING AGENCY REPORT NUMBER**
NASA TP-3440

**11. SUPPLEMENTARY NOTES**

**12a. DISTRIBUTION/AVAILABILITY STATEMENT**

Unclassified–Unlimited

Subject Category 02

**12b. DISTRIBUTION CODE**

**13. ABSTRACT** *(Maximum 200 words)*
An experimental investigation was performed in the Langley 16-Foot Transonic Tunnel to determine the effects of external and internal flap rippling on the aerodynamics of a nonaxisymmetric nozzle. Data were obtained at several Mach numbers from static conditions to 1.2 over a range of nozzle pressure ratios. Nozzles with chordal boattail angles of 10°, 20°, and 30°, with and without surface rippling, were tested. No effect on discharge coefficient due to surface rippling was observed. Internal thrust losses due to surface rippling were measured and attributed to a combination of additional internal skin friction and shock losses. External nozzle drag for the baseline configurations were generally less than that for the rippled configurations at all free-stream Mach numbers tested. The difference between the baseline and rippled nozzle drag levels generally increased with increasing boattail angle. The thrust-minus-drag level for each rippled nozzle configuration was less than the equivalent baseline configuration for each Mach number at the design nozzle pressure ratio.

**14. SUBJECT TERMS**
Aerodynamics; Two-dimensional convergent-divergent; Nozzles; Propulsion integration; Afterbody; Transonic; Mixer; Drag reduction; Separation control

**15. NUMBER OF PAGES**
108

**16. PRICE CODE**
A06

| 17. SECURITY CLASSIFICATION OF REPORT<br>Unclassified | 18. SECURITY CLASSIFICATION OF THIS PAGE<br>Unclassified | 19. SECURITY CLASSIFICATION OF ABSTRACT<br>Unclassified | 20. LIMITATION OF ABSTRACT |
|---|---|---|---|

NSN 7540-01-280-5500